

Pure kinetic inductance coupling for cQED with flux qubits

Simon Geisert,¹ Soeren Ihssen,^{1,*} Patrick Winkel,^{1,2,3} Martin Spiecker,¹ Mathieu Fechant,¹
 Patrick Paluch,^{1,4} Nicolas Gosling,¹ Nicolas Zapata,¹ Simon Günzler,¹ Dennis Rieger,^{1,4}
 Denis Bénâtre,¹ Thomas Reisinger,¹ Wolfgang Wernsdorfer,^{1,4} and Ioan M. Pop^{1,4,5,†}

¹*IQMT, Karlsruhe Institute of Technology, 76131 Karlsruhe, Germany*

²*Departments of Applied Physics and Physics, Yale University, New Haven, CT, USA*

³*Yale Quantum Institute, Yale University, New Haven, CT, USA*

⁴*PHI, Karlsruhe Institute of Technology, 76131 Karlsruhe, Germany*

⁵*Physics Institute 1, Stuttgart University, 70569 Stuttgart, Germany*

(Dated: September 12, 2024)

We demonstrate a qubit-readout architecture where the dispersive coupling is entirely mediated by a kinetic inductance. This allows us to engineer the dispersive shift of the readout resonator independent of the qubit and resonator capacitances. We validate the pure kinetic coupling concept and demonstrate various generalized flux qubit regimes from plasmon to fluxon, with dispersive shifts ranging from 60 kHz to 2 MHz at the half-flux quantum sweet spot. We achieve readout performances comparable to conventional architectures with quantum state preparation fidelities of 99.7% and 92.7% for the ground and excited states, respectively, and below 0.1% leakage to non-computational states.

The ability to convert model Hamiltonians into programmable physical systems is a stepping stone for quantum information processing. Circuit quantum electrodynamics (cQED) has been at the forefront of quantum hardware development over the past two decades [1, 2], benefitting from the freedom to design various micro-electronic circuit elements such as qubits, control, readout and coupler structures from the same basic building blocks. This has led to the development of increasingly complex quantum processors [3–7] and facilitated the exploration of fundamental quantum effects [8–14].

Dispersive coupling between qubits and harmonic oscillators is a pivotal resource for cQED, enabling single shot readout [15–18], the creation of non-classical photonic states [19, 20], reservoir engineering for qubit state preparation [21, 22] and even the autonomous stabilisation of entangled states [23]. Conventionally, dispersive coupling is mediated via electromagnetic interaction, most commonly using the electric field and a coupling capacitor. However, in complex devices, stray capacitors inevitably introduce unwanted cross-talk, renormalize the dispersive shift and even induce undesired electromotive forces across non-linear elements in the presence of alternating magnetic fields or field gradients [24]. In order to reduce the number of spurious electromagnetic modes and parasitic capacitances, several mitigation strategies are currently being developed in the community, including deep silicon vias [25–27], flip chip architectures [4, 5, 26, 28] and chiplets [29, 30].

Here, we present an alternative coupling approach that implements dispersive readout via pure kinetic inductance coupling between a generalized flux qubit and a harmonic oscillator and enables the complete suppression of capacitive coupling. We achieve this by designing

a three-island circuit with two normal modes, i.e. qubit and resonator, coupled solely by a kinetic inductance. While the kinetic inductance can be realized with Josephson junction (JJ) arrays, we demonstrate the concept with a high kinetic inductance material, namely granular aluminum (grAl) [31, 32]. The circuit’s symmetry effectively eliminates capacitive contributions to the qubit-readout interaction, rendering the coupling local.

To design the qubit-readout coupling we follow three design rules that will be expanded in the following paragraphs. First, we use the minimally required complexity for two electromagnetic modes, i.e. three circuit nodes. Second, we allocate different roles to the common and differential modes to implement the resonator and qubit. The qubit mode is obtained by connecting two nodes with a JJ. The electromagnetic mode that charges these nodes out of phase inherits a large anharmonicity from the JJ, while the orthogonal in-phase mode remains harmonic. Third, electric field coupling between the resonator and the qubit is eliminated by enforcing symmetric capacitors for the circuit nodes connecting the JJ, resulting in a permutation invariance of the capacitance matrix for these nodes.

In Fig. 1a we present our lumped-element circuit design which consists of three superconducting islands, i.e. circuit nodes **1**, **2** and **3**, connected via kinetic inductors made of grAl. The resulting superconducting loop, interrupted by the JJ and threaded by external flux Φ_{ext} , implements a generalized flux qubit (GFQ) [33]. The loop inductance L_q defines the inductive energy $E_L = \Phi_0^2/4\pi^2 L_q$ of the qubit, where $\Phi_0 = h/2e$ is the magnetic flux quantum.

If the circuit is symmetric with respect to the vertical symmetry line through node **3**, which means that nodes **1** and **2** have equal capacitances C_r as well as equal inductances $L_q/2$, the qubit and resonator modes are electromagnetically uncoupled. The main stray capacitances of the design are discussed in App. A.

* First two authors contributed equally.

† ioan.pop@kit.edu

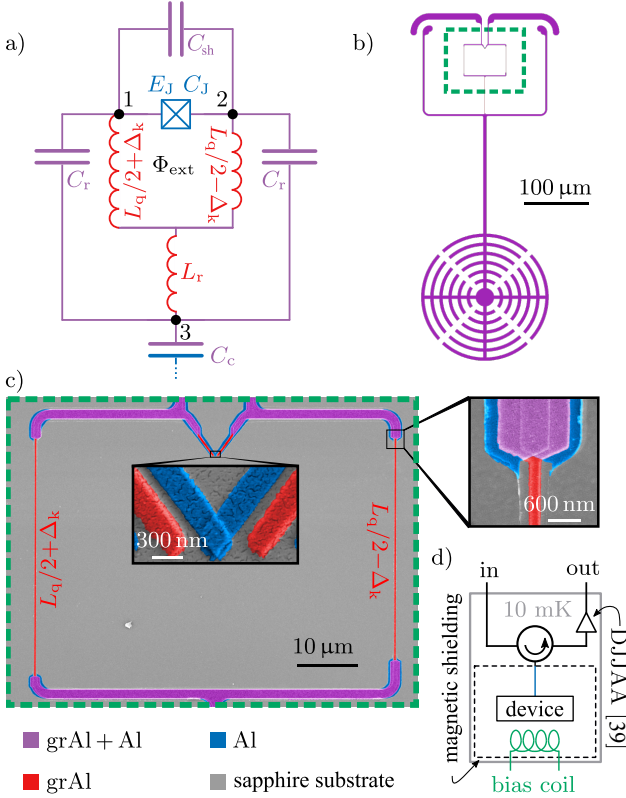


Figure 1. Qubit-readout circuit schematics and implementation. **a)** The islands of the device are labeled by the indices 1-3. Islands 1 and 2 are connected by a tunnel junction with Josephson energy E_J and capacitance C_J , shunted by a grAl inductance L_q and a capacitance C_{sh} , to form a generalized flux qubit. By connecting the third island to the qubit loop via the inductance L_r , we engineer the readout mode that charges the islands 1 and 2 in-phase. The qubit-readout coupling is controlled via the inductance asymmetry Δ_k between the loop branches. The capacitances C_r load the readout mode and C_c couples the circuit to the readout port. The colors indicate the materials used: blue for aluminum, red for grAl and purple for aluminum covered with grAl as a result of the three-angle fabrication process. **b)** Design layout of the device. The C_c pad has a skeletal shape to minimize screening currents and trapped vortices. **c)** False-coloured scanning electron micrograph of the qubit loop. By adjusting the length and width of the grAl strips the resonator frequency, coupling strength and qubit spectrum can be tuned independently. The insets show the Al/ AlO_x /Al junction with an area of $A_J \approx 0.06 \mu m^2$ and a section of the grAl wire. The grainy texture is due to a gold film deposited for imaging. **d)** Schematics of the microwave reflection measurement setup at 10 mK.

The current in the readout mode splits between the qubit loop branches and in case of perfect symmetry the net shared current with the qubit mode is zero. To engineer qubit-readout coupling we introduce the kinetic inductive asymmetry $\Delta_k = \Delta_\square L_\square/2$ by designing different grAl inductor lengths for the two qubit inductors in the qubit loop with a total difference of Δ_\square squares

of grAl wire with sheet inductance L_\square . In case of JJ arrays, this would translate into using different junction numbers or junction sizes for the two inductors. As a result, the readout mode current splits unevenly in the qubit loop and the circuit is equivalent to an inductively coupled qubit [34], where Δ_k plays the role of the shared inductance.

In contrast to capacitive [35, 36] or conventional inductive [31, 34] coupling of flux qubits, one circuit node is eliminated by collapsing the readout mode into the qubit loop. We would like to highlight several practical advantages of this coupling scheme. First, removing a circuit node pushes the parasitic modes to higher frequencies, improving the spectral purity of the device. Second, by coupling the resonator mode capacitively to a readout line using the capacitance C_c at node 3, the direct coupling of the qubit mode remains minimal thanks to the axial symmetry. Third, the qubit-resonator coupling can be designed to be purely inductive, loosening constraints on capacitor design, and possibly facilitating innovative flux-pumping schemes [24].

We model the Fig. 1a circuit in the harmonic oscillator basis of the linearized circuit eigenmodes:

$$\mathcal{H} = \hbar\omega_R \left(\hat{a}_R^\dagger \hat{a}_R + \frac{1}{2} \right) + \hbar\omega_Q \left(\hat{a}_Q^\dagger \hat{a}_Q + \frac{1}{2} \right) - E_J \cos \left(\lambda_R (\hat{a}_R + \hat{a}_R^\dagger) + \lambda_Q (\hat{a}_Q + \hat{a}_Q^\dagger) - \frac{2\pi}{\Phi_0} \Phi_{ext} \right), \quad (1)$$

where E_J is the Josephson energy, and $\hat{a}_{R,Q}^\dagger$ and $\hat{a}_{R,Q}$ are the bosonic creation and annihilation operators for the readout and qubit modes with eigenfrequencies ω_R and ω_Q , calculated without the Josephson inductance. The qubit and readout modes are linear combinations of the common and differential modes, defined by the dimensionless coupling coefficients $\lambda_{R,Q}$, derived in App. A. If we neglect the nonlinearity of the granular aluminum wire, the JJ is the sole source of nonlinearity in the system, such that the intuitive picture of a nonlinear qubit and linear readout mode is justified for $\lambda_R \ll \lambda_Q$. Note that the coupling between readout and qubit vanishes for perfect symmetry, i.e. $\lambda_R \rightarrow 0$ for $\Delta_k \rightarrow 0$.

In Fig. 1b we show the layout of the qubit-resonator design. A scanning electron micrograph of the qubit loop is shown in Fig. 1c. The qubit parameters can be tuned independently by adapting the length of the inductor L_q , the junction area defining E_J and C_J , and the size of the shunt capacitor electrodes determining C_{sh} . This can be done entirely geometrically, without changing the circuit topology nor the oxidation parameters for the JJ or the grAl film. The lateral inset in Fig. 1c shows a section of the grAl wire. Thanks to the relatively large kinetic inductance offered by grAl [37, 38], it is sufficient to add a few squares of grAl film to one qubit branch to span the range from zero up to several nH of inductive asymmetry Δ_k . Notably, this can be done with minimal disturbance to the geometric inductance and the capacitance matrix.

The central inset of Fig. 1c shows a scanning electron micrograph of the qubit $\text{Al}/\text{AlO}_x/\text{Al}$ junction. The entire device is fabricated on a c-plane sapphire substrate in a single lithographic step using a three-angle shadow evaporation technique, similar to Ref. [31]. The aluminum layers (20 nm and 30 nm) are shadow evaporated to define the junction, followed by a zero-angle deposition of a 70 nm layer of grAl with resistivities between $450 \mu\Omega\text{cm}$ and $1000 \mu\Omega\text{cm}$ depending on the device (cf. App. B). The sample is mounted in a modular flip-chip architecture, anchored to the base plate of a dilution-cryostat at approx. 10 mK and it is measured in reflection, as shown in Fig. 1d. The output signal is amplified using a dimer Josephson junction array amplifier (DJ-JAA) [39] operating close to the quantum noise limit.

We measure the spectra of 14 different GFQs as a function of the external flux Φ_{ext} using two-tone spectroscopy. A typical spectrum is shown in Fig. 2a. Using the circuit Hamiltonian in Eq. 1 we fit the qubit and resonator spectra simultaneously to obtain the circuit parameters L_r , L_q , Δ_k , C_J and E_J , while capacitors C_r and C_{sh} are inferred from finite-element simulations (see App. D). The coupling asymmetry Δ_k is determined by the width of the avoided level crossing and L_q , C_J and E_J are given by the measured qubit level structure.

The qubit spectra can be understood in terms of universal double-well physics [33], ranging from the fluxon-tunneling regime $E_J > E_L$ in which the barrier height exceeds the confining quadratic potential, to the single-well plasmon regime for $E_J < E_L$. As summarized in Fig. 2b, the distribution of qubit frequencies and anharmonicities follow the underlying single and double-well physics: Towards the plasmon regime, the qubit frequencies increase whereas the anharmonicities decrease. Towards the fluxon regime, frequencies decrease while anharmonicities increase as expected from the exponential scaling of the qubit frequency with the barrier height [40]. At half-flux bias we measure coherence times in the range of 1 μs to 10 μs , likely limited by inductive losses in grAl as summarized in App. E.

In Fig. 2c we compare the fitted and designed coupling asymmetry Δ_k . The qubit-readout coupling is given by the sum of designed inductive coupling via Δ_k and spurious capacitive asymmetries, which we parametrize as $\Delta_C = (C_{13} - C_{23})/2$. These asymmetries can arise from asymmetric spurious capacitances of islands **1** and **2** to ground. From finite-element simulations we estimate a maximal value of $\Delta_C = \pm 25 \text{ aF}$ due to a possible asymmetric displacement of the qubit chip with respect to ground. The corresponding uncertainties in the extraction of Δ_k are given as errorbars in Fig. 2c.

The dispersive shift of the readout resonator is

$$\chi = (E_{|1,1\rangle} - E_{|0,1\rangle}) / h - (E_{|1,0\rangle} - E_{|0,0\rangle}) / h,$$

where $E_{|n_R, n_Q\rangle}$ is the energy level sorted by the readout (n_R) and qubit (n_Q) photon number. In Fig. 2d we compare the measured dispersive shifts to the expected model values using the extracted Δ_k from spectroscopic

measurements for nine qubits. The measured data is consistent with circuit model predictions for $\Delta_C = 0$, validating the pure kinetic inductance coupling design.

To quantify the readout performance of our device we have performed two sets of characterization: contiguous measurement correlations and active state reset, with pulse sequences detailed in Fig. 3a & e, respectively. We define the signal to noise ratio (SNR) in the I - Q plane of the readout mode as the distance between pointer states corresponding to qubit in $|0\rangle$ and $|1\rangle$, divided by the sum of their standard deviations. In all experiments we fix $\text{SNR} \approx 3.7$, which is obtained by adjusting the integration times $t_{\text{int}} \in (1600, 208) \text{ ns}$ depending on the different average photon numbers $\bar{n} \in (10, 150)$ in the resonator.

In Fig. 3b we show an example section of a contiguously measured quantum jump trace for GFQ device q7. By applying a Gaussian mixture model to quantum jump traces with 10^6 points for a given \bar{n} , we extract qubit populations in $|0\rangle$, $|1\rangle$ and $|2^+\rangle$ (see Fig. 3c) and correlations P_{00} and P_{11} for two successive measurements in the ground and excited state (see Fig. 3d), respectively. The correlations P_{00} and P_{11} serve as a measure of qubit readout fidelity, particularly useful to assess quantum demolition effects introduced by the readout drive. Similarly to Ref. [41], the resilience of the grAl GFQ to readout-induced leakage [42–44] is illustrated by the fact that up to $\bar{n} \approx 100$, the qubit populations remain approximately constant, corresponding to an effective temperature of about 40 mK to 45 mK and residual excitations outside of the computational subspace remain below 0.1 %.

Within the qubit subspace, we observe a significant difference in the correlation of successive readout outcomes when the qubit is in the ground or excited state. Qubit measurements in the ground state are highly correlated, with $P_{00} > 99.9\%$ for a broad range of readout powers. In contrast, we find that P_{11} depends on the readout strength, with $P_{11} \geq 90\%$ for $\bar{n} \in (75, 140)$. The difference between the measured P_{11} and perfect correlation can be accounted for by summing three contributions: Energy decay during the measurement reduces P_{11} by $1 - \exp(-t_{\text{int}}/T_1)$, which for $t_{\text{int}} = 352 \text{ ns}$ can be as high as 6 % given the measured $T_1 = 8.0 \pm 2.4 \mu\text{s}$ for device q7. Second, the qubit spectral shift and broadening induced by the readout tone will change the dissipative environment of the qubit [45] and might accelerate the relaxation from the excited to the ground state. The third contribution comes from demolishing effects activated when increasing \bar{n} [46], such as leakage outside of the qubit subspace [42]. The second and third contributions, which sum up to give at least 4% of the P_{11} infidelity, provide a measure for the performance of the qubit-readout coupling scheme and motivate future research efforts.

We implement active state preparation starting from the thermal state of the qubit by playing a conditional π -pulse. The threshold to discriminate states $|0\rangle$ and $|1\rangle$ is determined by measuring the I - Q plane distribu-

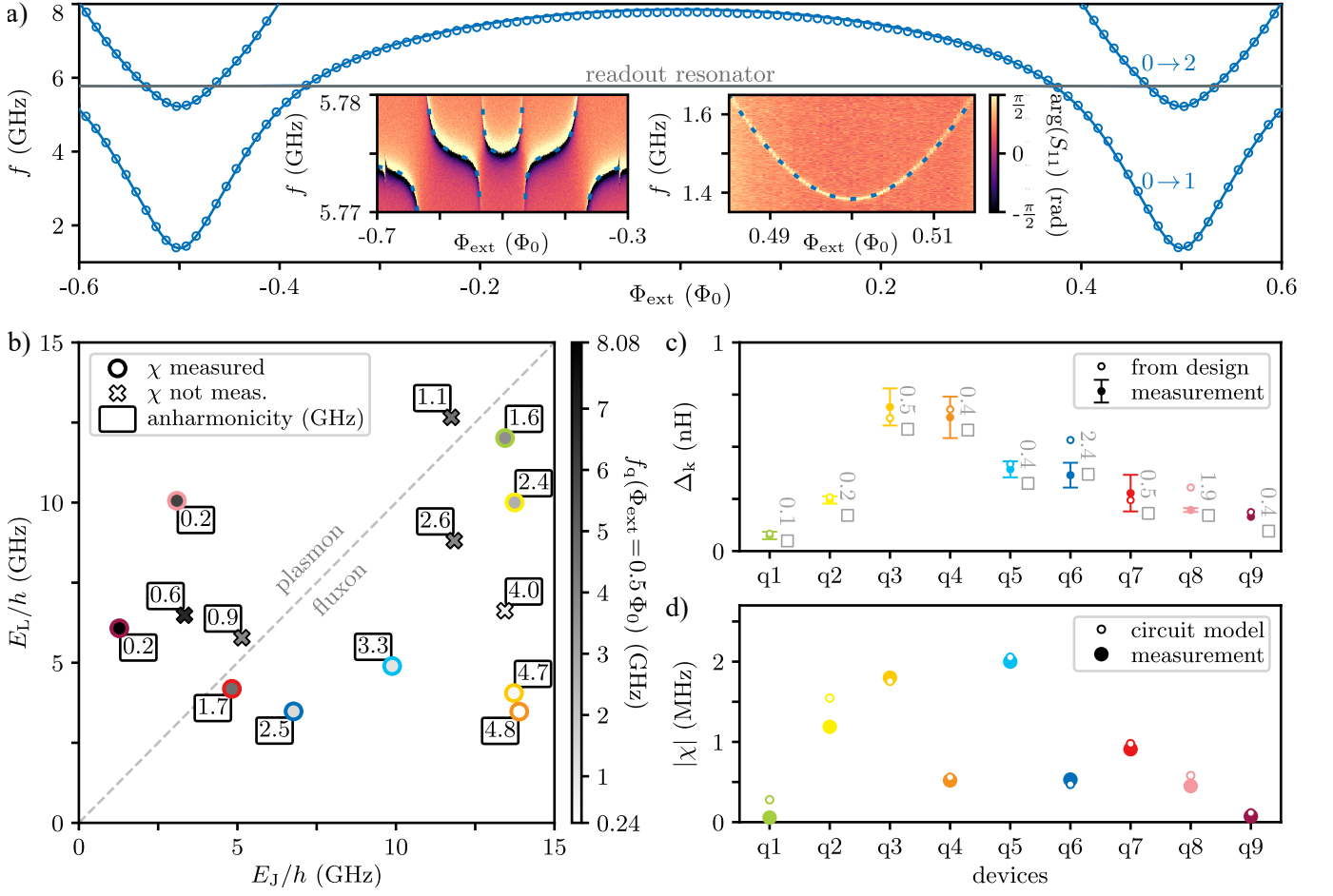


Figure 2. From plasmon to fluxon: summary of measured qubit parameters. **a)** Combined plot of typical single and two tone spectroscopy of $0 \rightarrow 1$ and $0 \rightarrow 2$ qubit transitions (blue circles) vs. flux bias Φ_{ext} of device q6 as well as the 5.77 GHz resonance of the readout resonator (grey horizontal line). The inset on the left shows the measured phase response $\arg(S_{11})$ of the readout mode in the vicinity of the qubit-readout avoided level crossings when probing the system with a single tone. The inset on the right shows the phase response of the resonator on resonance when probing the qubit with a second tone near the qubit frequency in the vicinity of the half-flux sweet spot $\Phi_{\text{ext}} = \Phi_0/2$. The blue lines (dashed and continuous) correspond to the fitted circuit model with fit parameters E_J , L_q , L_r , C_J and Δ_k . **b)** Phase diagram E_L vs. E_J for the measured GFQs. The grey-scale intensity of the marker filler indicates the $0 \rightarrow 1$ transition frequency f_q at the half-flux point, with corresponding labels indicating the anharmonicity. The diagonal grey line separates the plasmon regime on the left from the fluxon regime on the right. Devices for which the dispersive shift χ was measured (was not measured) have a circular (cross-shaped) marker. **c)** Qubit loop asymmetry Δ_k for selected devices. The filled circles indicate the values of Δ_k extracted from the joint fit of the qubit and resonator spectroscopy (cf. left inset of panel **a** and App. C). The errorbars correspond to possible capacitive coupling arising from asymmetries $\Delta_C = \pm 25 \text{ aF} < 0.01 \cdot C_r$ in the capacitance matrix. The design values, shown as empty circles, are given by the product of the sheet inductance and the length difference between the qubit branches. The sheet inductance is extracted from the fitted L_q and the designed number of squares in the loop. The discrepancy between the measured and design values is shown in grey labels in units of squares. The marker color assigned to each sample is consistent in all panels. **d)** Qubit state dependent dispersive shift χ at $\Phi_{\text{ext}} = \Phi_0/2$ for selected devices. Filled circles show χ values extracted from complex plane distributions of single shot measurements (cf. App. C). Empty circles indicate the calculated χ assuming pure kinetic inductance coupling.

tions after a saturation pulse, as shown in Fig. 3f. Using $\bar{n} = 85$, the fidelities to reset the qubit to its ground and excited state read $P_0^{\text{active}} = 99.7\%$ and $P_1^{\text{active}} = 92.7\%$, respectively (cf. Fig. 3g & h). In the error budget for quantum state preparation, the fidelity of the π -pulse of $>99\%$ (cf. App. F) is a negligible contribution com-

pared to the decay during readout and quantum demolition effects. The measured performance for our GFQ devices are similar to results reported for fluxoniums and transmons [41, 47, 48] but below state-of-the-art fidelity reaching 99% [49]. Currently, the main limitation for the readout performance is the energy relaxation time of the

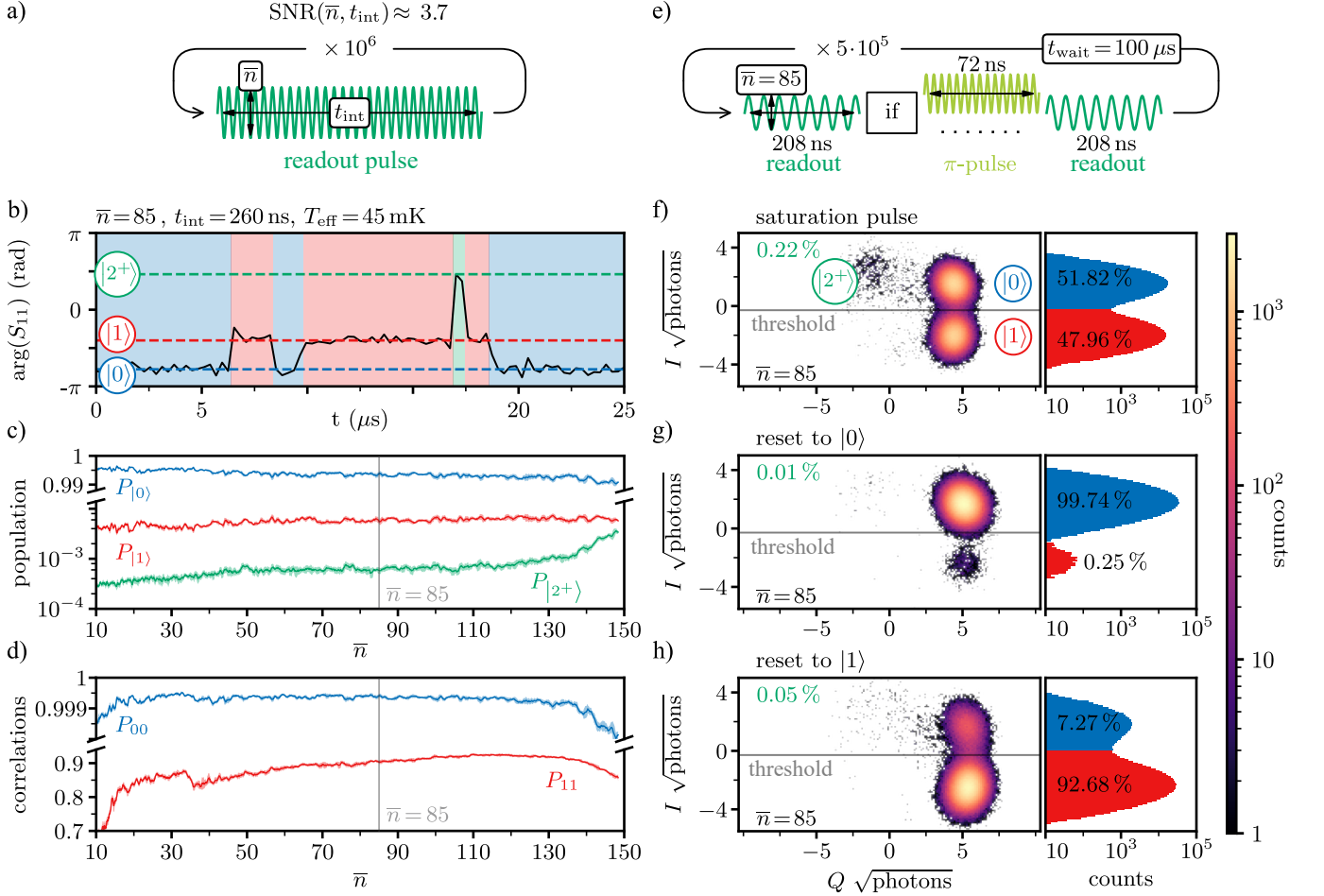


Figure 3. **Readout fidelity and quantum state preparation.** **a)** Pulse sequence for the continuous-wave measurement protocol: 10^6 contiguous readout pulses are sent and integrated for different photon numbers \bar{n} . For each \bar{n} , the integration time t_{int} is adapted to keep the $\text{SNR} = 3.7 \pm 0.2$. **b)** Typical quantum jump trajectory visible in the measured phase of the reflection coefficient S_{11} shown in a window of 25 μs for device q7. The qubit states are assigned using a Gaussian mixture model and indicated by the color of the background: blue ($|0\rangle$ = ground), red ($|1\rangle$ = excited) and green ($|2^+\rangle$ = other). **c)** Measured states population vs. \bar{n} . Note that leakage to the $|2^+\rangle$ -states accelerates for $\bar{n} \gtrsim 130$. **d)** Correlation P_{xx} for consecutive measurements in the ground ($x=0$) or excited ($x=1$) state vs. \bar{n} . The minimal integration time, 200 ns, is approximately three times larger than the resonator response time. **e)** Pulse sequence used for active state reset. The measurement outcome of the first readout pulse is used to condition a π -pulse on the qubit. The result of the second readout is used to assess the fidelity of the reset protocol. We use $\bar{n} = 85$ and $t_{\text{int}} = 208$ ns resulting in a state separation of $\approx 6\sigma$. We repeat the sequence 5×10^5 times with a waiting time of $t_{\text{wait}} = 100$ μs in between. The measured pointer state distributions for 50 % polarization, active reset to $|0\rangle$ and $|1\rangle$ are shown in panels **f**, **g** and **h**, respectively. The grey line is the threshold used for state assignment in the active reset protocol. The green label indicates leakage into higher states. The measurement outcomes are depicted as histograms in logarithmic scale.

qubit, which can be significantly improved via material and design optimization [50].

We have demonstrated dispersive coupling between a harmonic mode and a generalized flux qubit consisting of a single junction shunted by a granular aluminum inductor. By embedding the harmonic readout mode into the high kinetic inductance loop of the flux qubit we implement a mechanism conceptually equivalent to inductive coupling, where the loop asymmetry is equivalent to the shared inductance. We validate the kinetic inductance coupling concept by comparing the spectra of 14 devices

obtained via two-tone spectroscopy to a model including parasitic capacitances. We assess the suitability of the coupling mechanism for dispersive readout by performing quantum non-demolition readout with $> 90\%$ active state preparation fidelity and less than 0.1 % leakage outside the qubit computational space. Thanks to its ability to provide a local qubit-resonator interaction unaffected by on-chip capacitors, we believe that the minimalist qubit-resonator design presented here will provide an advantageous avenue for up-scaling superconducting quantum devices.

ACKNOWLEDGEMENTS

We are grateful to L. Radtke and S. Diewald for technical assistance. We acknowledge funding from the European Commission (FET-Open AVaQus GA 899561). Facilities use was supported by the KIT Nanostructure Service Laboratory. We acknowledge the measurement software framework qKit. The authors acknowledge support by the state of Baden-Württemberg through bwHPC. M.S., P.P, N.G. and T.R. acknowledge support

from the German Ministry of Education and Research (BMBF) within the project GEQCOS (FKZ: 13N15683). D.B. and M.F. acknowledge funding from the German Federal Ministry of Education and Research (BMBF) within the project QSolid (FKZ: 13N16151). N.Z. acknowledges funding from the Deutsche Forschungsgemeinschaft (DFG – German Research Foundation) under project number 450396347 (GeHoldeQED). S.Gü., D.R. and W.W. acknowledge support from the Leibniz award WE 4458-5.

-
- [1] A. Wallraff, D. I. Schuster, A. Blais, L. Frunzio, R.-S. Huang, J. Majer, S. Kumar, S. M. Girvin, and R. J. Schoelkopf, Strong coupling of a single photon to a superconducting qubit using circuit quantum electrodynamics, *Nature* **431**, 162 (2004).
 - [2] A. Blais, A. L. Grimsmo, S. M. Girvin, and A. Wallraff, Circuit quantum electrodynamics, *Rev. Mod. Phys.* **93**, 025005 (2021).
 - [3] Y. Sung, L. Ding, J. Braumüller, A. Vepsäläinen, B. Kannan, M. Kjaergaard, A. Greene, G. O. Samach, C. McNally, D. Kim, A. Melville, B. M. Niedzielski, M. E. Schwartz, J. L. Yoder, T. P. Orlando, S. Gustavsson, and W. D. Oliver, Realization of high-fidelity *cz* and *zz*-free swap gates with a tunable coupler, *Phys. Rev. X* **11**, 021058 (2021).
 - [4] C. R. Conner, A. Bienfait, H.-S. Chang, M.-H. Chou, É. Dumur, J. Grebel, G. A. Pears, R. G. Povey, H. Yan, Y. P. Zhong, and A. N. Cleland, Superconducting qubits in a flip-chip architecture, *Appl. Phys. Lett.* **118**, 10.1063/5.0050173 (2021).
 - [5] S. Kosen, H.-X. Li, M. Rommel, D. Shiri, C. Warren, L. Grönberg, J. Salonen, T. Abad, J. Biznárová, M. Caputo, L. Chen, K. Grigoras, G. Johansson, A. F. Kockum, C. Križan, D. P. Lozano, G. J. Norris, A. Osman, J. Fernández-Pendás, A. Ronzani, A. F. Roudsari, S. Simbierowicz, G. Tancredi, A. Wallraff, C. Eichler, J. Govenius, and J. Bylander, Building blocks of a flip-chip integrated superconducting quantum processor, *Quantum Science and Technology* **7**, 035018 (2022).
 - [6] Y. Wu, W.-S. Bao, S. Cao, F. Chen, M.-C. Chen, X. Chen, T.-H. Chung, H. Deng, Y. Du, D. Fan, M. Gong, C. Guo, C. Guo, S. Guo, L. Han, L. Hong, H.-L. Huang, Y.-H. Huo, L. Li, N. Li, S. Li, Y. Li, F. Liang, C. Lin, J. Lin, H. Qian, D. Qiao, H. Rong, H. Su, L. Sun, L. Wang, S. Wang, D. Wu, Y. Xu, K. Yan, W. Yang, Y. Yang, Y. Ye, J. Yin, C. Ying, J. Yu, C. Zha, C. Zhang, H. Zhang, K. Zhang, Y. Zhang, H. Zhao, Y. Zhao, L. Zhou, Q. Zhu, C.-Y. Lu, C.-Z. Peng, X. Zhu, and J.-W. Pan, Strong quantum computational advantage using a superconducting quantum processor, *Phys. Rev. Lett.* **127**, 180501 (2021).
 - [7] F. Arute, K. Arya, R. Babbush, D. Bacon, J. C. Bardin, R. Barends, R. Biswas, S. Boixo, F. G. S. L. Brandao, D. A. Buell, B. Burkett, Y. Chen, Z. Chen, B. Chiaro, R. Collins, W. Courtney, A. Dunsworth, E. Farhi, B. Foxen, A. Fowler, C. Gidney, M. Giustina, R. Graff, K. Guerin, S. Habegger, M. P. Harrigan, M. J. Hartmann, A. Ho, M. Hoffmann, T. Huang, T. S. Humble, S. V. Isakov, E. Jeffrey, Z. Jiang, D. Kafri, K. Kechedzhi, J. Kelly, P. V. Klimov, S. Knysh, A. Korotkov, F. Kostritsa, D. Landhuis, M. Lindmark, E. Lucero, D. Lyakh, S. Mandrà, J. R. McClean, M. McEwen, A. Megrant, X. Mi, K. Michielsen, M. Mohseni, J. Mutus, O. Naaman, M. Neeley, C. Neill, M. Y. Niu, E. Ostby, A. Petukhov, J. C. Platt, C. Quintana, E. G. Rieffel, P. Roushan, N. C. Rubin, D. Sank, K. J. Satzinger, V. Smelyanskiy, K. J. Sung, M. D. Trevithick, A. Vainsencher, B. Villalonga, T. White, Z. J. Yao, P. Yeh, A. Zalcman, H. Neven, and J. M. Martinis, Quantum supremacy using a programmable superconducting processor, *Nature* **574**, 505 (2019).
 - [8] P. Campagne-Ibarcq, P. Six, L. Bretheau, A. Sarlette, M. Mirrahimi, P. Rouchon, and B. Huard, Observing quantum state diffusion by heterodyne detection of fluorescence, *Phys. Rev. X* **6**, 011002 (2016).
 - [9] Z. K. Mineev, S. O. Mundhada, S. Shankar, P. Reinhold, R. Gutiérrez-Jáuregui, R. J. Schoelkopf, M. Mirrahimi, H. J. Carmichael, and M. H. Devoret, To catch and reverse a quantum jump mid-flight, *Nature* **570**, 200 (2019).
 - [10] S. Léger, J. Puertas-Martínez, K. Bharadwaj, R. Dassonneville, J. Delaforce, F. Foroughi, V. Milchakov, L. Planat, O. Buisson, C. Naud, W. Hasch-Guichard, S. Florens, I. Snyman, and N. Roch, Observation of quantum many-body effects due to zero point fluctuations in superconducting circuits, *Nature Communications* **10**, 10.1038/s41467-019-13199-x (2019).
 - [11] J. Stevens, D. Szombati, M. Maffei, C. Elouard, R. Assouly, N. Cottet, R. Dassonneville, Q. Ficheux, S. Zepetbauer, A. Bienfait, A. N. Jordan, A. Auffèves, and B. Huard, Energetics of a single qubit gate, *Phys. Rev. Lett.* **129**, 110601 (2022).
 - [12] S. Chakram, K. He, A. V. Dixit, A. E. Oriani, R. K. Naik, N. Leung, H. Kwon, W.-L. Ma, L. Jiang, and D. I. Schuster, Multimode photon blockade, *Nature Physics* **18**, 879 (2022).
 - [13] N. Mehta, R. Kuzmin, C. Ciuti, and V. E. Manucharyan, Down-conversion of a single photon as a probe of many-body localization, *Nature* **613**, 650 (2023).
 - [14] N. Roch, M. E. Schwartz, F. Motzoi, C. Macklin, R. Vijay, A. W. Eddins, A. N. Korotkov, K. B. Whaley, M. Sarovar, and I. Siddiqi, Observation of measurement-induced entanglement and quantum trajectories of remote superconducting qubits, *Phys. Rev. Lett.* **112**, 170501 (2014).

- [15] R. Vijay, D. H. Slichter, and I. Siddiqi, Observation of Quantum Jumps in a Superconducting Artificial Atom, *Phys. Rev. Lett.* **106**, 110502 (2011).
- [16] J. Heinsoo, C. K. Andersen, A. Remm, S. Krinner, T. Walter, Y. Salathé, S. Gasparinetti, J.-C. Besse, A. Potočnik, A. Wallraff, and C. Eichler, Rapid High-fidelity Multiplexed Readout of Superconducting Qubits, *Phys. Rev. Appl.* **10**, 034040 (2018).
- [17] F. Swiadek, R. Shillito, P. Magnard, A. Remm, C. Hellings, N. Lacroix, Q. Ficheux, D. C. Zanuz, G. J. Norris, A. Blais, S. Krinner, and A. Wallraff, Enhancing Dispersive Readout of Superconducting Qubits Through Dynamic Control of the Dispersive Shift: Experiment and Theory, *arXiv 10.48550/arXiv.2307.07765* (2023), 2307.07765.
- [18] I. Takmakov, P. Winkel, F. Foroughi, L. Planat, D. Gusenkova, M. Spiecker, D. Rieger, L. Grünhaupt, A. V. Ustinov, W. Wernsdorfer, I. M. Pop, and N. Roch, Minimizing the Discrimination Time for Quantum States of an Artificial Atom, *Phys. Rev. Appl.* **15**, 064029 (2021).
- [19] M. Hofheinz, H. Wang, M. Ansmann, R. C. Bialczak, E. Lucero, M. Neeley, A. D. O'Connell, D. Sank, J. Wenner, J. M. Martinis, and A. N. Cleland, Synthesizing arbitrary quantum states in a superconducting resonator, *Nature* **459**, 546 (2009).
- [20] G. Kirchmair, B. Vlastakis, Z. Leghtas, S. E. Nigg, H. Paik, E. Ginossar, M. Mirrahimi, L. Frunzio, S. M. Girvin, and R. J. Schoelkopf, Observation of quantum state collapse and revival due to the single-photon Kerr effect, *Nature* **495**, 205 (2013).
- [21] K. Geerlings, Z. Leghtas, I. M. Pop, S. Shankar, L. Frunzio, R. J. Schoelkopf, M. Mirrahimi, and M. H. Devoret, Demonstrating a Driven Reset Protocol for a Superconducting Qubit, *Phys. Rev. Lett.* **110**, 120501 (2013).
- [22] K. W. Murch, U. Vool, D. Zhou, S. J. Weber, S. M. Girvin, and I. Siddiqi, Cavity-Assisted Quantum Bath Engineering, *Phys. Rev. Lett.* **109**, 183602 (2012).
- [23] S. Shankar, M. Hatridge, Z. Leghtas, K. M. Sliwa, A. Narla, U. Vool, S. M. Girvin, L. Frunzio, M. Mirrahimi, and M. H. Devoret, Autonomously stabilized entanglement between two superconducting quantum bits, *Nature* **504**, 419 (2013).
- [24] Y. Lu, A. Maiti, J. W. O. Garmon, S. Ganjam, Y. Zhang, J. Claes, L. Frunzio, S. M. Girvin, and R. J. Schoelkopf, High-fidelity parametric beamsplitting with a parity-protected converter, *Nat. Commun.* **14**, 1 (2023).
- [25] J. P. Gambino, S. A. Adderly, and J. U. Knickerbocker, An overview of through-silicon-via technology and manufacturing challenges, *Microelectronic Engineering* **135**, 73 (2015).
- [26] D. R. W. Yost, M. E. Schwartz, J. Mallek, D. Rosenberg, C. Stull, J. L. Yoder, G. Calusine, M. Cook, R. Das, A. L. Day, E. B. Golden, D. K. Kim, A. Melville, B. M. Niedzielski, W. Woods, A. J. Kerman, and W. D. Oliver, Solid-state qubits integrated with superconducting through-silicon vias, *npj Quantum Information* **6**, 10.1038/s41534-020-00289-8 (2020).
- [27] J. A. Alfaro-Barrantes, M. Mastrangeli, D. J. Thoen, S. Visser, J. Bueno, J. J. A. Baselmans, and P. M. Sarro, Highly-conformal sputtered through-silicon vias with sharp superconducting transition, *Journal of Microelectromechanical Systems* **30**, 253 (2021).
- [28] J. Yu, Y. Zheng, S. Zhou, Q. Wang, S. Wu, H. Wu, T. Li, and J. Cai, Indium-based flip-chip interconnection for superconducting quantum computing application, in *2022 23rd International Conference on Electronic Packaging Technology (ICEPT)* (2022) pp. 1–6.
- [29] K. N. Smith, G. S. Ravi, J. M. Baker, and F. T. Chong, Scaling superconducting quantum computers with chiplet architectures, in *2022 55th IEEE/ACM International Symposium on Microarchitecture (MICRO)* (2022) pp. 1092–1109.
- [30] M. Field, A. Q. Chen, B. Scharmann, E. A. Sete, F. Oruc, K. Vu, V. Kosenko, J. Y. Mutus, S. Poletto, and A. Bestwick, Modular superconducting-qubit architecture with a multichip tunable coupler, *Phys. Rev. Appl.* **21**, 054063 (2024).
- [31] L. Grünhaupt, M. Spiecker, D. Gusenkova, N. Maleeva, S. T. Skacel, I. Takmakov, F. Valenti, P. Winkel, H. Rotzinger, W. Wernsdorfer, A. V. Ustinov, and I. M. Pop, Granular aluminium as a superconducting material for high-impedance quantum circuits, *Nature Materials* **18**, 816–819 (2019).
- [32] D. Rieger, S. Günzler, M. Spiecker, P. Paluch, P. Winkel, L. Hahn, J. K. Hohmann, A. Bacher, W. Wernsdorfer, and I. M. Pop, Granular aluminium nanojunction fluxonium qubit, *Nature Materials* **22**, 194 (2022).
- [33] F. Yan, Y. Sung, P. Krantz, A. Kamal, D. K. Kim, J. L. Yoder, T. P. Orlando, S. Gustavsson, and W. D. Oliver, Engineering Framework for Optimizing Superconducting Qubit Designs, *arXiv 10.48550/arXiv.2006.04130* (2020), 2006.04130.
- [34] W. C. Smith, A. Kou, U. Vool, I. M. Pop, L. Frunzio, R. J. Schoelkopf, and M. H. Devoret, Quantization of inductively shunted superconducting circuits, *Phys. Rev. B* **94**, 144507 (2016).
- [35] V. E. Manucharyan, J. Koch, L. I. Glazman, and M. H. Devoret, Fluxonium: Single Cooper-Pair Circuit Free of Charge Offsets, *Science* **326**, 113 (2009).
- [36] F. Bao, H. Deng, D. Ding, R. Gao, X. Gao, C. Huang, X. Jiang, H.-S. Ku, Z. Li, X. Ma, X. Ni, J. Qin, Z. Song, H. Sun, C. Tang, T. Wang, F. Wu, T. Xia, W. Yu, F. Zhang, G. Zhang, X. Zhang, J. Zhou, X. Zhu, Y. Shi, J. Chen, H.-H. Zhao, and C. Deng, Fluxonium: An alternative qubit platform for high-fidelity operations, *Phys. Rev. Lett.* **129**, 010502 (2022).
- [37] H. Rotzinger, S. T. Skacel, M. Pfirrmann, J. N. Voss, J. Münzberg, S. Probst, P. Bushev, M. P. Weides, A. V. Ustinov, and J. E. Mooij, Aluminium-oxide wires for superconducting high kinetic inductance circuits, *Supercond. Sci. Technol.* **30**, 025002 (2016).
- [38] L. Grünhaupt, N. Maleeva, S. T. Skacel, M. Calvo, F. Levy-Bertrand, A. V. Ustinov, H. Rotzinger, A. Monfardini, G. Catelani, and I. M. Pop, Loss mechanisms and quasiparticle dynamics in superconducting microwave resonators made of thin-film granular aluminum, *Phys. Rev. Lett.* **121**, 117001 (2018).
- [39] P. Winkel, I. Takmakov, D. Rieger, L. Planat, W. Hasch-Guichard, L. Grünhaupt, N. Maleeva, F. Foroughi, F. Henriques, K. Borisov, J. Ferrero, A. V. Ustinov, W. Wernsdorfer, N. Roch, and I. M. Pop, Nondegenerate parametric amplifiers based on dispersion-engineered josephson-junction arrays, *Phys. Rev. Appl.* **13**, 024015 (2020).
- [40] G. Rastelli, I. M. Pop, and F. W. J. Hekking, Quantum phase slips in josephson junction rings, *Phys. Rev. B* **87**,

- 174513 (2013).
- [41] D. Gusenkova, M. Spiecker, R. Gebauer, M. Willsch, D. Willsch, F. Valenti, N. Karcher, L. Grünhaupt, I. Takmakov, P. Winkel, D. Rieger, A. V. Ustinov, N. Roch, W. Wernsdorfer, K. Michielsen, O. Sander, and I. M. Pop, Quantum nondemolition dispersive readout of a superconducting artificial atom using large photon numbers, *Phys. Rev. Appl.* **15**, 064030 (2021).
 - [42] M. F. Dumas, B. Groleau-Paré, A. McDonald, M. H. Muñoz-Arias, C. Lledó, B. D'Anjou, and A. Blais, Unified picture of measurement-induced ionization in the transmon, *arXiv 10.48550/arXiv.2402.06615* (2024), 2402.06615.
 - [43] R. Shillito, A. Petrescu, J. Cohen, J. Beall, M. Hauru, M. Ganahl, A. G. Lewis, G. Vidal, and A. Blais, Dynamics of transmon ionization, *Phys. Rev. Appl.* **18**, 034031 (2022).
 - [44] J. Cohen, A. Petrescu, R. Shillito, and A. Blais, Reminiscence of classical chaos in driven transmons, *PRX Quantum* **4**, 020312 (2023).
 - [45] T. Thorbeck, Z. Xiao, A. Kamal, and L. C. G. Govia, Readout-induced suppression and enhancement of superconducting qubit lifetimes, *Phys. Rev. Lett.* **132**, 090602 (2024).
 - [46] T. Walter, P. Kurpiers, S. Gasparinetti, P. Magnard, A. Potočnik, Y. Salathé, M. Pechal, M. Mondal, M. Oppliger, C. Eichler, and A. Wallraff, Rapid High-Fidelity Single-Shot Dispersive Readout of Superconducting Qubits, *Phys. Rev. Appl.* **7**, 054020 (2017).
 - [47] M. O. Tholén, R. Borgani, G. R. Di Carlo, A. Bengtsson, C. Križan, M. Kudra, G. Tancredi, J. Bylander, P. Delsing, S. Gasparinetti, and D. B. Haviland, Measurement and control of a superconducting quantum processor with a fully integrated radio-frequency system on a chip, *Rev. Sci. Instrum.* **93**, 10.1063/5.0101398 (2022).
 - [48] D. Ristè, C. C. Bultink, K. W. Lehnert, and L. DiCarlo, Feedback control of a solid-state qubit using high-fidelity projective measurement, *Phys. Rev. Lett.* **109**, 240502 (2012).
 - [49] Y. Sunada, S. Kono, J. Ilves, S. Tamate, T. Sugiyama, Y. Tabuchi, and Y. Nakamura, Fast readout and reset of a superconducting qubit coupled to a resonator with an intrinsic purcell filter, *Phys. Rev. Appl.* **17**, 044016 (2022).
 - [50] I. Siddiqi, Engineering high-coherence superconducting qubits, *Nat. Rev. Mater.* **6**, 875 (2021).
 - [51] M. Rymarz and D. P. DiVincenzo, Consistent quantization of nearly singular superconducting circuits, *Phys. Rev. X* **13**, 021017 (2023).

APPENDIX

A. Circuit Models

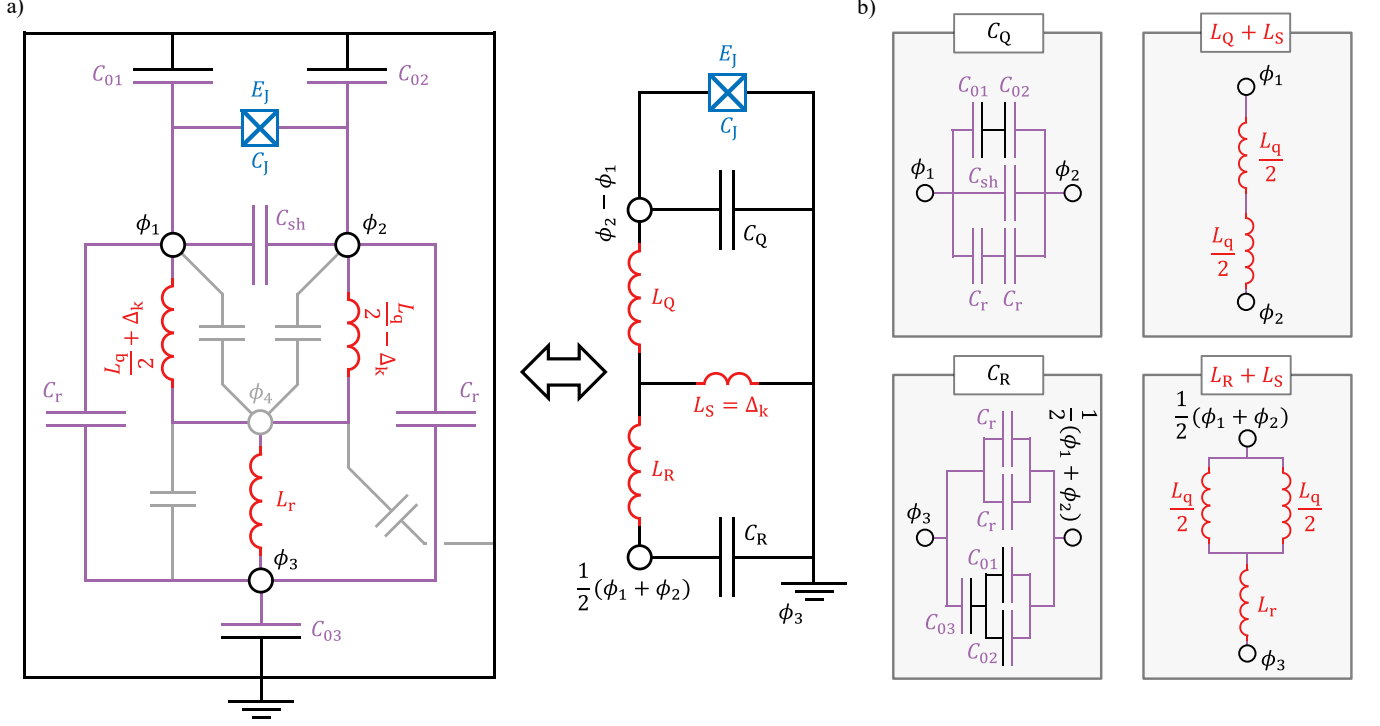


Figure S1. **Extended and idealized circuit model.** a) In addition to islands **1** to **3** discussed in the main text, the extended circuit model describes all four islands (black empty circles) including island **4**, which is marked in grey. Blue, purple and red colors indicate the materials used, consistent with Fig. 1 in the main text. Neglecting the influence of island **4** and assuming symmetric capacitances, the extended circuit is equivalent to an idealized inductively coupled circuit via the shared inductance $L_S = \Delta_k$, in which $L_{Q,R}$ and $C_{Q,R}$ are the equivalent inductance and capacitance of the qubit and resonator, respectively. b) The four panels depict the transformations required to obtain the equivalent circuit branch components C_Q , C_R , L_Q and L_R .

The circuit is modeled in terms of the flux node variables $\vec{\phi}^T = (\phi_1, \phi_2, \phi_3, \phi_4)$ and illustrated in Fig. S1. Following the canonical circuit quantization procedure, the Lagrangian reads

$$\begin{aligned} \mathcal{L} &= \frac{1}{2} \dot{\vec{\phi}}^T \mathbf{C} \dot{\vec{\phi}} + \frac{1}{2} \vec{\phi}^T \mathbf{L}^{-1} \vec{\phi} + E_J \cos \left(\frac{2\pi}{\Phi_0} (\phi_2 - \phi_1 - \Phi_{\text{ext}}) \right) \\ &= \mathcal{L}_{\text{lin}} + E_J \cos \left(\frac{2\pi}{\Phi_0} (\phi_2 - \phi_1 - \Phi_{\text{ext}}) \right). \end{aligned} \quad (\text{S1})$$

where \mathcal{L}_{lin} is the linearized circuit Lagrangian without the junction cosine potential, Φ_{ext} is the external flux through the qubit loop, \mathbf{C} is the capacitance matrix and \mathbf{L}^{-1} the inverse inductance matrix, given by

$$\mathbf{C} = \begin{pmatrix} C_{11} + C_J & -C_{12} - C_J & -C_{13} & -C_{14} \\ -C_{12} - C_J & C_{22} + C_J & -C_{23} & -C_{24} \\ -C_{13} & -C_{23} & C_{33} & -C_{34} \\ -C_{14} & -C_{24} & -C_{34} & C_{44} \end{pmatrix}$$

and

$$\mathbf{L}^{-1} = \begin{pmatrix} \frac{1}{L_q/2+\Delta} & 0 & 0 & \frac{-1}{L_q/2+\Delta} \\ 0 & \frac{1}{L_q/2-\Delta} & 0 & \frac{-1}{L_q/2-\Delta} \\ 0 & 0 & \frac{1}{L_r} & \frac{-1}{L_r} \\ \frac{-1}{L_q/2+\Delta} & \frac{-1}{L_q/2-\Delta} & \frac{-1}{L_r} & \frac{1}{L_q/2+\Delta} + \frac{1}{L_q/2-\Delta} + \frac{1}{L_r} \end{pmatrix}.$$

The capacitances C_{ij} are obtained by finite-element simulations and include the capacitances between the islands on the chip and the sample holder (ground) C_{i0} . The junction parallel plate capacitance C_J is excluded from the simulations and enters as an additional capacitance between nodes **1** and **2**. A possible misalignment of the floating chip with respect to the symmetric sample holder environment gives the capacitive asymmetry

$$\Delta_C = \frac{C_{13}-C_{23}}{2}.$$

Extended circuit model

We start with a coordinate transformation from $\vec{\phi}$ to $\vec{x} = \mathbf{C}^{1/2}\vec{\phi}$, in which the linearized Lagrangian reads

$$\mathcal{L}_{\text{lin}} = \frac{1}{2}\dot{\vec{x}}^\top \dot{\vec{x}} - \frac{1}{2}\vec{x}^\top \mathbf{C}^{-\frac{1}{2}} \mathbf{L}^{-1} \mathbf{C}^{-\frac{1}{2}} \vec{x}.$$

The bare normal modes $\vec{\eta}_j$ are then found by solving the eigenvalue problem

$$\mathbf{C}^{-\frac{1}{2}} \mathbf{L}^{-1} \mathbf{C}^{-\frac{1}{2}} \vec{\eta}_j = \omega_j^2 \vec{\eta}_j$$

via the transformation matrix $\mathbf{S} = (\vec{\eta}_1, \vec{\eta}_2, \vec{\eta}_3, \vec{\eta}_4)$, such that the eigenbasis is written as $\vec{\eta} = (\eta_1, \eta_2, \eta_3, \eta_4)^\top = \mathbf{S}^\top \vec{x}$. By introducing the conjugate momenta $p_i = \frac{\partial \mathcal{L}_{\text{lin}}}{\partial \dot{\eta}_i}$ we obtain the diagonal linearized Hamiltonian

$$\mathcal{H}_{\text{lin}} = \sum_i p_i \dot{\eta}_i - \mathcal{L}_{\text{lin}} = \frac{1}{2} \sum_i (p_i^2 + \omega_i^2 \eta_i^2).$$

The eigenmodes are sorted with respect to their even and odd amplitudes across the junction, meaning that the qubit mode is defined as $\eta_Q = \eta_1$ with $|\mathbf{S}_{21} - \mathbf{S}_{11}| > |\mathbf{S}_{2j} - \mathbf{S}_{1j}| \forall j \neq 1$ and the readout mode as $\eta_R = \eta_2$ with $|\mathbf{S}_{22} + \mathbf{S}_{12}| > |\mathbf{S}_{2j} + \mathbf{S}_{1j}| \forall j \neq 2$. The back transformation from the harmonic oscillator (H.O) basis to the original flux node variables then reads

$$\vec{\phi} = \underbrace{\mathbf{C}^{-\frac{1}{2}} \mathbf{S}}_{\mathbf{S}'} \vec{\eta}.$$

The common and differential modes can then be expressed in terms of qubit and readout modes as

$$\begin{aligned} \phi_2 - \phi_1 &\approx (\mathbf{S}'_{2Q} - \mathbf{S}'_{1Q}) \eta_Q + (\mathbf{S}'_{2R} - \mathbf{S}'_{1R}) \eta_R \\ \phi_2 + \phi_1 &\approx (\mathbf{S}'_{2Q} + \mathbf{S}'_{1Q}) \eta_Q + (\mathbf{S}'_{2R} + \mathbf{S}'_{1R}) \eta_R \end{aligned} \tag{S2}$$

where we neglect the presence of the zero mode and the higher frequency mode associated with island **4**. This simplification [51] is justified in our case because the mode associated with island **4**, at ≈ 30 GHz, is sufficiently detuned from the spectrum of the device to give negligible corrections.

In the H.O. basis, coupling is solely mediated by the junction cosine term driven by the differential mode. To quantify it, we express the cosine argument in Eq. S1 via the above transformation and quantize the qubit-readout system and apply the canonical quantization procedure to the qubit and readout variables

$$\begin{aligned} \eta_{R,Q} &= \sqrt{\frac{\hbar}{2\omega_{R,Q}}} \left(\hat{a}_{R,Q} + \hat{a}_{R,Q}^\dagger \right) \\ p_{R,Q} &= i \sqrt{\frac{\hbar\omega_{R,Q}}{2}} \left(\hat{a}_{R,Q}^\dagger - \hat{a}_{R,Q} \right). \end{aligned}$$

Using this procedure we obtain the main text Hamiltonian

$$\begin{aligned}\mathcal{H} = & \hbar\omega_R \left(\hat{a}_R^\dagger \hat{a}_R + \frac{1}{2} \right) + \hbar\omega_Q \left(\hat{a}_Q^\dagger \hat{a}_Q + \frac{1}{2} \right) \\ & - E_J \cos \left(\lambda_R (\hat{a}_R + \hat{a}_R^\dagger) + \lambda_Q (\hat{a}_Q + \hat{a}_Q^\dagger) - \frac{2\pi}{\Phi_0} \Phi_{\text{ext}} \right)\end{aligned}$$

with

$$\lambda_R = \frac{2\pi}{\Phi_0} \sqrt{\frac{\hbar}{2\omega_R}} (\mathbf{S}'_{2R} - \mathbf{S}'_{1R}) \quad \lambda_Q = \frac{2\pi}{\Phi_0} \sqrt{\frac{\hbar}{2\omega_Q}} (\mathbf{S}'_{2Q} - \mathbf{S}'_{1Q}).$$

To obtain the qubit-resonator spectrum, we numerically diagonalize the Hamiltonian in the photon number basis using 15 and 30 basis states for the resonator and qubit, respectively.

Idealized circuit model

While the procedure discussed in the previous section is sufficient to calculate the qubit-resonator spectrum, in order to gain intuition on the current and future designs, we find it instructive to also discuss the idealized model for a symmetric capacitive environment with $\Delta_C = 0$. Below, we simplify the linearized extended circuit model in terms of the flux nodes $\vec{\phi}^\top = (\phi_1, \phi_2)$, c.f. Eq. S2. Neglecting the capacitances to the center node **4**, we can eliminate this inactive node via Kirchhoff's rule of conserved currents

$$\frac{\phi_4 - \phi_3}{L_r} = \frac{\phi_2 - \phi_4}{\frac{L_q}{2} - \Delta_k} + \frac{\phi_1 - \phi_4}{\frac{L_q}{2} + \Delta_k}.$$

Further removing the zero mode with respect to the sample holder (ground), we can gauge $\phi_3 = 0$ as the new reference potential and write

$$\phi_4 = \Sigma_L^{-1} \left(L_r \left(\frac{L_q}{2} + \Delta_k \right) \phi_2 + L_r \left(\frac{L_q}{2} - \Delta_k \right) \phi_1 \right) \quad (\text{S3})$$

where we define

$$\Sigma_L = L_r L_q + \frac{L_q^2}{4} - \Delta_k^2.$$

The inductive contribution to the Lagrangian is

$$U = \frac{1}{2L_r} \phi_4^2 + \frac{1}{2 \left(\frac{L_q}{2} + \Delta_k \right)} (\phi_1 - \phi_4)^2 + \frac{1}{2 \left(\frac{L_q}{2} - \Delta_k \right)} (\phi_2 - \phi_4)^2.$$

Using Eq. S3,

$$U = \frac{1}{2\Sigma_L} \left(\left(L_r + \left(\frac{L_q}{2} - \Delta_k \right) \right) \phi_1^2 + \left(L_r + \left(\frac{L_q}{2} + \Delta_k \right) \right) \phi_2^2 - 2L_r \phi_1 \phi_2 \right),$$

which can be rewritten in matrix form as $U = \frac{1}{2} \vec{\phi}^\top \mathbf{L}^{-1} \vec{\phi}$, with the inverse inductance matrix

$$\mathbf{L}^{-1} = \frac{1}{\Sigma_L} \begin{pmatrix} L_r + \frac{L_q}{2} - \Delta_k & -L_r \\ -L_r & L_r + \frac{L_q}{2} + \Delta_k \end{pmatrix}.$$

To account for the contribution of the stray capacitances to ground, we treat the ground as a free node with conserved charge with respect to the floating islands and eliminate it from the Lagrangian by writing

$$\dot{\phi}_0 = \frac{C_{J0}}{C_{30} + 2C_{J0}} (\dot{\phi}_1 + \dot{\phi}_2),$$

where $C_{J0} = C_{10} = C_{20}$ is the junction electrode capacitance to ground. The capacitive contribution to the Lagrangian then is

$$T = \frac{1}{2} \left(C_r + C_{sh} + C_{J0} - \frac{C_{J0}^2}{C_{30} + 2C_{J0}} \right) (\dot{\phi}_1^2 + \dot{\phi}_2^2) - \left(C_{sh} + \frac{C_{J0}^2}{C_{30} + 2C_{J0}} \right) \dot{\phi}_1 \dot{\phi}_2$$

which can be rewritten in matrix form as $T = \frac{1}{2} \dot{\vec{\phi}}^T \mathbf{C} \dot{\vec{\phi}}$, with the capacitance matrix

$$\mathbf{C} = \begin{pmatrix} C_r + C_{sh} + C_{J0} - \frac{C_{J0}^2}{C_{30} + 2C_{J0}} & -C_{sh} - \frac{C_{J0}^2}{C_{30} + 2C_{J0}} \\ -C_{sh} - \frac{C_{J0}^2}{C_{30} + 2C_{J0}} & C_r + C_{sh} + C_{J0} - \frac{C_{J0}^2}{C_{30} + 2C_{J0}} \end{pmatrix}.$$

For $\Delta_k = 0$, a transformation that diagonalizes both \mathbf{C} and \mathbf{L}^{-1} simultaneously is

$$\begin{aligned} \phi_Q &= \phi_2 - \phi_1 \\ \phi_R &= \frac{1}{2}(\phi_1 + \phi_2), \end{aligned}$$

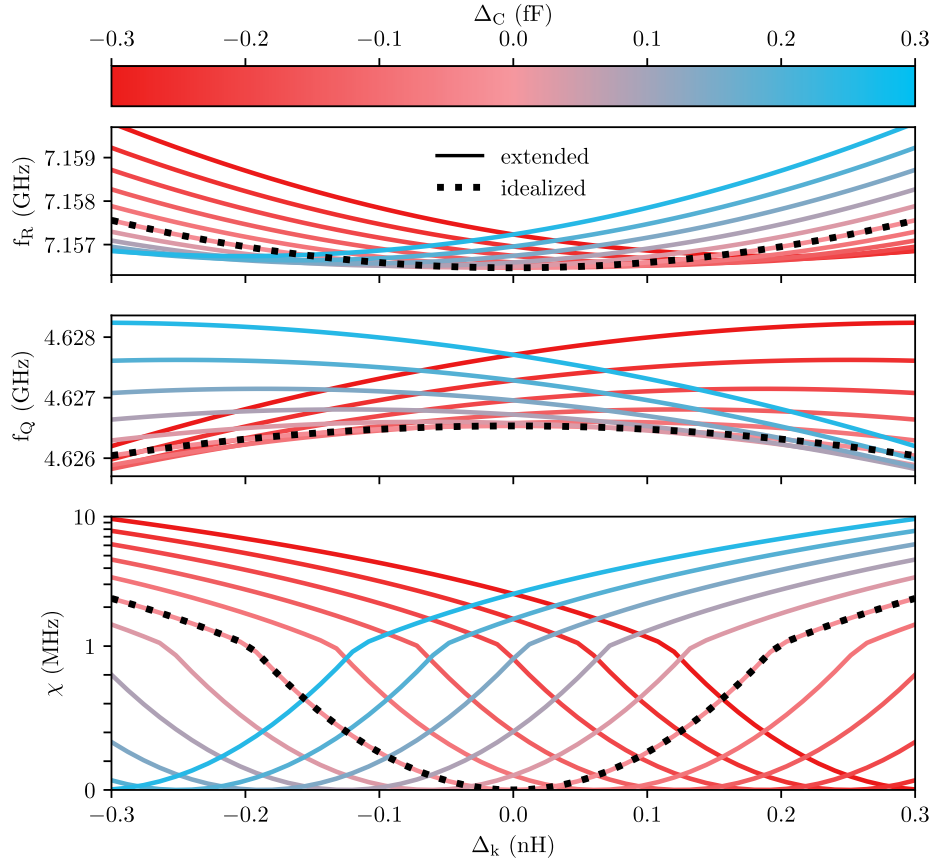


Figure S2. **Numerical comparison between the extended and idealized circuit model and the effect of capacitive and inductive asymmetries.** The three plots calculated at $\phi_{\text{ext}} = \frac{\Phi_0}{2}$ as a function of inductive asymmetry Δ_k show, from top to bottom, the readout and qubit frequencies f_R and f_Q , respectively, and the dispersive shift. For $\Delta_C = 0$, the idealized model (dotted line) gives the same results as the extended model. For finite Δ_C , the capacitive coupling adds to the inductive coupling, introducing a shift in the curves. Notice that a fF of capacitive asymmetry roughly equals a nH of inductive asymmetry in terms of the resulting dispersive shift. Technologically relevant dispersive shifts on the order of MHz can be implemented with 100's of aF or 100's of pH asymmetry.

with the corresponding basis

$$\vec{\phi}^* = \begin{pmatrix} \phi_R \\ \phi_Q \end{pmatrix}.$$

Applying the above transformation for finite Δ_k yields the matrices in the new basis

$$\mathbf{L}^{*-1} = \frac{1}{\Sigma_L} \begin{pmatrix} L_q & -\Delta_k \\ -\Delta_k & L_r + \frac{L_q}{4} \end{pmatrix}$$

and

$$\mathbf{C}^* = \begin{pmatrix} 2C_r + \left(\frac{1}{2C_{J0}} + \frac{1}{C_{30}}\right)^{-1} & 0 \\ 0 & C_r/2 + C_{sh} + C_{J0}/2 \end{pmatrix}.$$

Finally, we define the qubit (Q) and readout (R) effective parameters, c.f Fig. S1b, as

$$\begin{aligned} L_Q &= L_q - \Delta_k \\ L_R &= L_r + \frac{L_q}{4} - \Delta_k \\ L_S &= \Delta_k \\ C_R &= 2C_r + \left(\frac{1}{2C_{J0}} + \frac{1}{C_{30}}\right)^{-1} \\ C_Q &= C_r/2 + C_{sh} + C_{J0}/2, \end{aligned}$$

such that the matrices can be rewritten as

$$\mathbf{L}^{*-1} = \frac{1}{L_R L_Q + L_R L_S + L_Q L_S} \begin{pmatrix} L_Q + L_S & -L_S \\ -L_S & L_R + L_S \end{pmatrix}$$

and

$$\mathbf{C}^* = \begin{pmatrix} C_R & 0 \\ 0 & C_Q \end{pmatrix},$$

as expected from the idealized inductively coupled circuit Fig. S1b which is similar to Ref. [41]. A numerical comparison between the idealized circuit and the extended circuit is shown in Fig. S2.

B. Fabrication

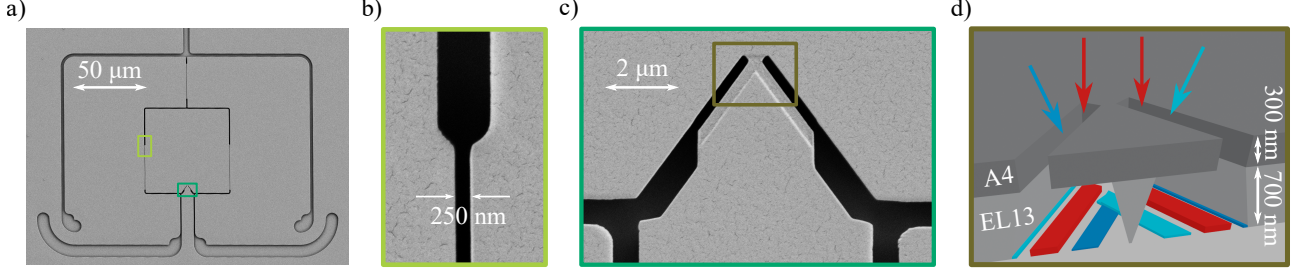


Figure S3. **Fabrication using a three-angle evaporation process.** **a)** Scanning electron microscope image of the device during fabrication after e-beam patterning and development of the two-layer resist stack. The surface is covered by a gold film for imaging. **b)** Zoom-in on the pattern defining the connection of the thin grAl inductor to the Al-shunted islands. **c)** Zoom-in on the cross-junction pattern used to fabricate the JJ. In the brown-highlighted area, an undercut is used to separate the Al depositions from the zero-angle grAl deposition. **d)** Sketch of the Dolan-bridge and the depositions of the three different layers of Al (blue) and grAl (red). The undercut in the EL-13 (700 nm) + PMMA-A4 (300 nm) resist stack allows to create the entire device in a single three-angle evaporation step with subsequent evaporation angles $-\alpha, 0^\circ, \alpha$, where $\alpha \in [26^\circ, 30^\circ]$, depending on the sample.

The devices are fabricated on a double-side polished c-plane 2 inch sapphire wafer with a thickness of $330 \mu\text{m}$. A two level resist stack MMA(8.5)MAA EL 13 (700 nm thick layer) / 950 PMMA A4 (300 nm thick layer) is spin-coated onto the wafer. An approx. 5 nm thick gold layer is sputtered onto the wafer before e-beam writing. A 50 keV e-beam writer is used to pattern the mask. After e-beam exposure a 15% Lugol solution is used to remove the gold. The resist stack is developed in an IPA/H₂O 3:1 solution at 6°C for 90 s. Images of the resulting mask are shown in Fig. S3a to Fig. S3c. A Niemeyer-Dolan bridge shown in Fig. S3c & d is used to fabricate the Josephson junction. A commercial, controlled-angle e-beam evaporation machine (Plassys MEB 550STM) is used to implement the three-angle evaporation process as shown in Fig. S3d. The evaporation steps are detailed in the paragraph below. For the mask liftoff, the wafer is immersed for two hours in a 60°C Acetone bath, which is stirred for 2 minutes every 20 minutes.

Evaporation procedure

The evaporation machine has two chambers. The first chamber is used as loadlock and for oxidation, while the second UHV chamber is used for evaporation. In detail the following steps are used during evaporation:

- Pump the loadlock for a minimum of 2 hours until the pressure is smaller than $5 \cdot 10^{-7}$ mbar.
- Plasma cleaning process at 0° angle (Kaufman source parameters: 200 V beam voltage, 10 mA, 10 sccm O₂, 5 sccm Ar)
- Titanium evaporation with closed shutter (10 s with 0.2 nm/s)
- Aluminium evaporation at $-\alpha$ with open shutter (Al crucible 1, 20 nm with 1 nm/s)
- Static oxidation (pure O₂) of Josephson junction at 50 mbar for 4 min (+20 s to linearly increase the pressure to 50 mbar)
- Aluminium evaporation at α with open shutter (Al crucible 1, 30 nm with 1 nm/s)
- Argon milling process at 0° angle (Kaufman source parameters: 400 V beam voltage, 15 mA, 0 sccm O₂, 4 sccm Ar)
- Regulate aluminium evaporation at 0° angle to 2 nm/s (Al crucible 2)
- Regulate oxygen flow to 9.4 sccm and start planetary rotation with 5 rpm

- Open shutter and evaporate for ~ 35 s (corresponds to 70 nm of grAl)
- Close shutter, terminate oxygen flow, stop planetary rotation, ramp down aluminium evaporation rate

Using the process described above grAl film resistivities at room temperature vary between $450 \mu\Omega\text{cm}$ and $1000 \mu\Omega\text{cm}$ as can be seen in Table S1.

Date	ρ [$\mu\Omega\text{cm}$]
Sep 2022	620
Sep 2022	660
Nov 2022	840
Nov 2022	940
Nov 2022	640
Dec 2022	880
Dec 2022	1000
Feb 2023	720
Mar 2023	530
Sep 2023	520
Dec 2023	470

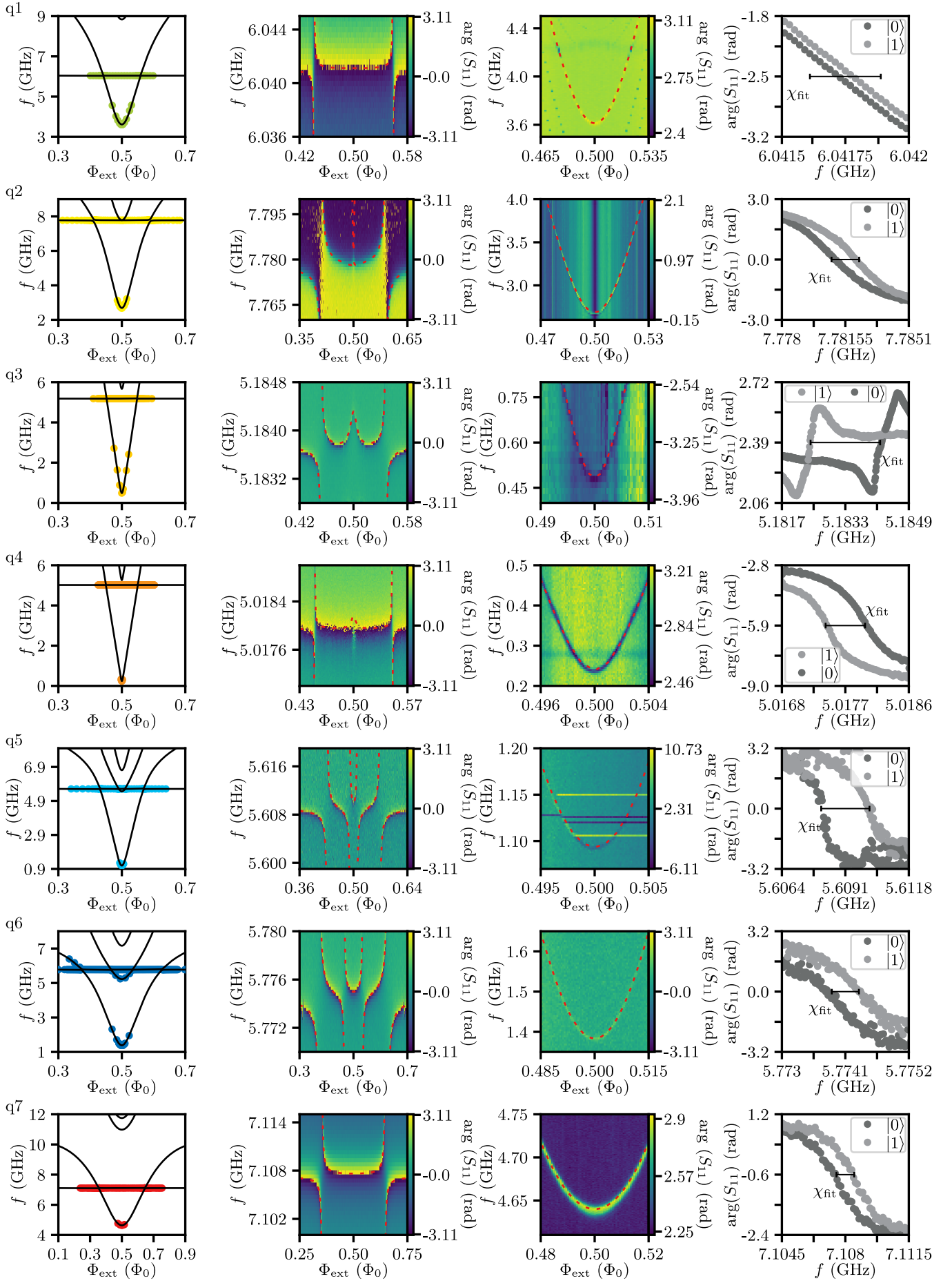
Table S1. **Resistivity of different grAl films at room temperature as a function of deposition date.** We use the same evaporation procedure for all grAl depositions and the thickness of the grAl film is 70 nm. The variability of grAl resistivity over timescales of months could be due to changes in the level of aluminum in the crucible, humidity or other cleanroom conditions.

C. Measured and fitted spectra

The circuit model described in App. A is fitted to the qubit spectra using a minimization method based on the python module `scipy.minimize`. In Fig. S4 the extracted data points are shown for each qubit. The resulting fit parameters L_q , L_r , Δ_k , E_J and C_J are listed in Table S2 for each qubit. The measured dispersive shift χ is compared to its calculated value in the columns 7 and 8 of Table S2.

device	L_r [nH]	L_q [nH]	Δ_k [nH]	E_J [GHz]	C_J [fF]	χ_{fit} [MHz]	χ_{meas} [MHz]
q1	15.03	13.61	-0.07	13.44	4.82	0.28	0.06
q2	6.53	16.34	-0.24	13.74	6.01	1.55	1.19
q3	29.36	40.35	0.69	13.72	3.78	-1.75	-1.80
q4	30.14	47.07	0.64	13.89	5.01	-0.56	-0.52
q5	11.90	33.38	0.39	9.88	4.02	2.05	2.00
q6	7.40	46.96	0.36	6.77	3.34	0.47	0.53
q7	11.73	39.06	0.28	4.83	1.85	0.98	0.91
q8	0.55	16.25	0.20	3.09	2.58	0.58	0.45
q9	18.89	26.91	0.17	1.28	1.86	0.11	0.07
q10	11.10	18.55	0.22	11.84	2.13	-	-
q11	9.82	12.91	-0.31	11.75	4.97	-	-
q12	6.54	24.68	-0.30	13.44	4.97	-	-
q13	7.60	28.28	0.86	5.14	4.37	-	-
q14	19.62	25.21	0.17	3.33	3.58	-	-

Table S2. **Device parameters obtained from the extended circuit model fit to the measured spectra (c.f. Fig. S4).**



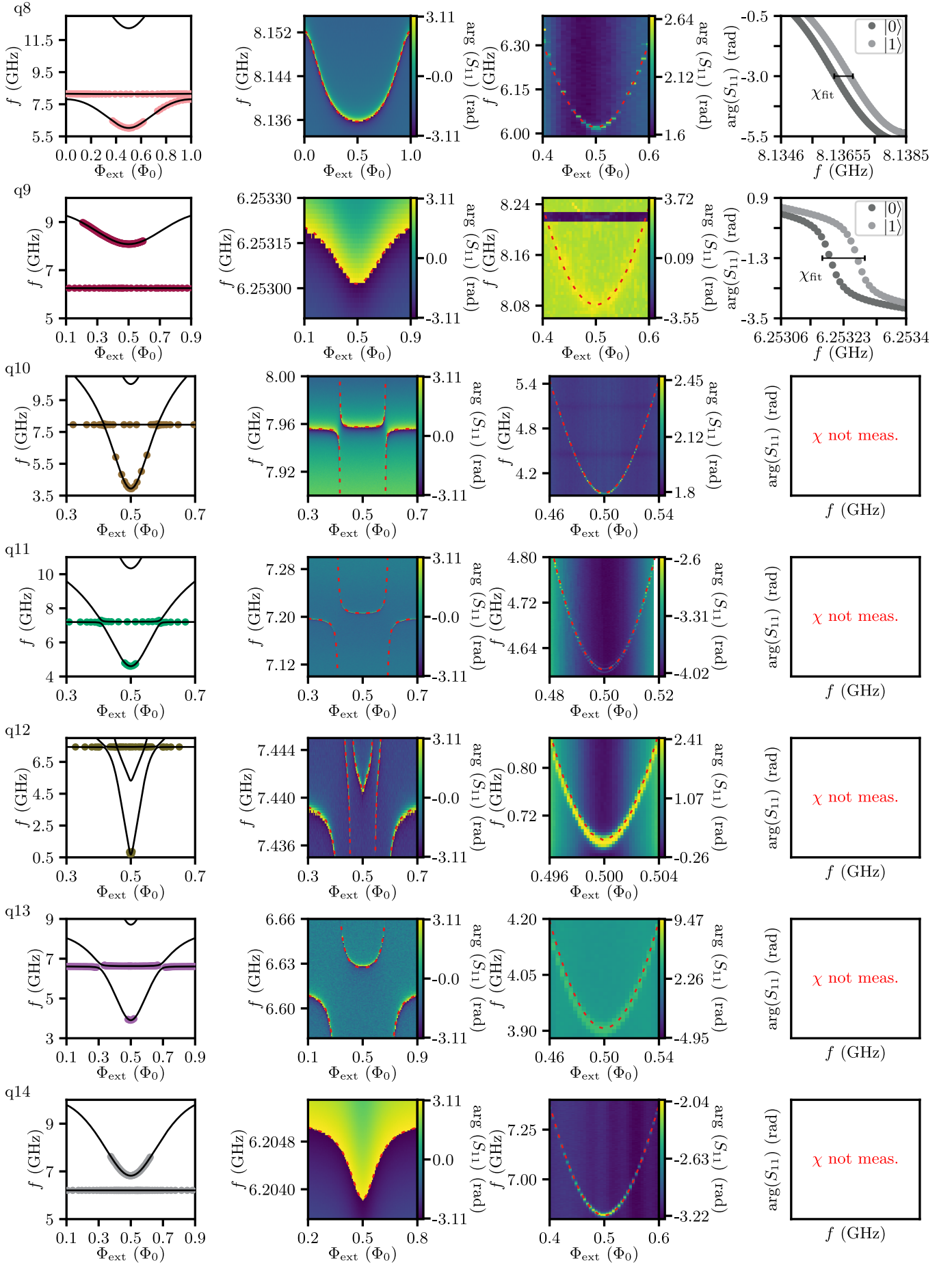


Figure S4. **Qubit spectra and dispersive shifts χ at $\Phi_{\text{ext}} = 0.5\Phi_0$.** In the first column plots the data points are extracted from single-tone and two-tone spectroscopy of the resonator and qubit, shown in column 2 and 3, respectively. The black lines show fits to the circuit model. The measured dispersive shifts plotted in the 4th column for devices q1 to q9 are extracted from pulsed single shot readout. The response of the resonator for the qubit in the ground (excited) state is shown in dark (light) grey markers. The χ value calculated from the circuit model is shown as a horizontal black line. The measured and calculated χ values are tabulated in Table S2.

D. Electrostatic finite-element simulations

To obtain the capacitance matrix \mathbf{C} , electrostatic simulations are conducted, for which the electrostatic finite element solver Ansys Maxwell is used. The simulations are performed with a detailed 3D model of the copper sample box with refined mesh regions used for finer structures, as can be seen in Fig. S5. The mesh is automatically generated and therefore not perfectly symmetric with respect to the islands **1** and **2** (see Fig. S5.b) leading to convergence errors of 10 aF for the simulated capacitances, which are listed in Table S3 for all simulated devices.

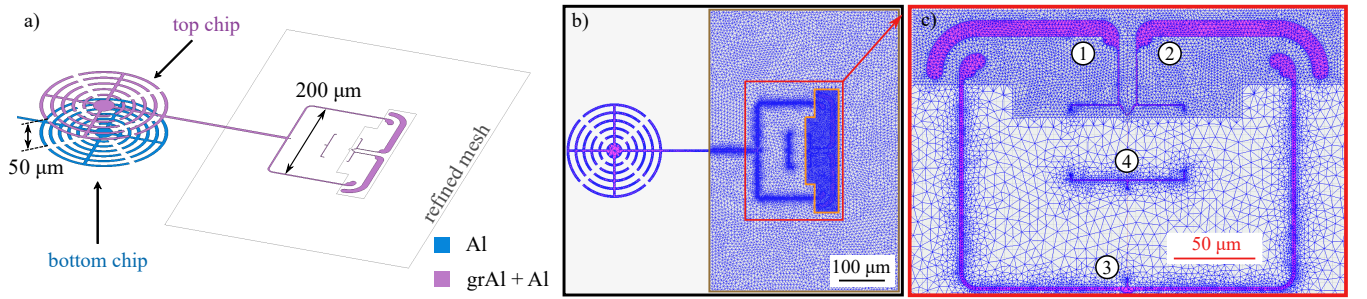


Figure S5. **Electrostatic finite element simulations with ANSYS Maxwell for the capacitance matrix \mathbf{C} .** **a)** Layout of the flip-chip assembly. The qubit-readout circuit is flipped above the bottom chip to form the parallel plate capacitor C_c (c.f. Fig. 1 in the main text) with a distance of approx. 50 μm between the chips. The readout line on the bottom chip is itself coupled capacitively to a coaxial cable (not shown) through which the system is measured in reflection. **b)** Mesh details of the qubit-readout system. The capacitive parts are colored in magenta. The mesh tetrahedra are superposed in blue. Refined mesh regions are used for the sensitive regions inside the brown and orange boxes. **b)** Zoom in on the qubit loop and capacitive structures of the qubit-readout system. The inductive parts and the junction are omitted in the simulation, leaving behind disconnected areas defining the circuit islands labeled by the node indices **1** to **4**. The mesh is generated automatically and is not perfectly symmetric with respect to islands **1** and **2**.

Qubit	C_{11} [fF]	C_{22} [fF]	C_{33} [fF]	C_{44} [fF]	$C_{12,21} = C_{\text{sh}}$ [fF]	$C_{24,42}$ [fF]	$C_{14,41}$ [fF]	$C_{23,32} = C_r$ [fF]	$C_{13,31} = C_r$ [fF]	$C_{34,43}$ [fF]
q1	33.42	33.28	99.36	2.92	11.77	0.29	0.29	8.63	8.67	0.84
q2	32.45	32.39	76.93	3.03	3.22	0.36	0.32	6.30	6.34	0.72
q3	16.47	16.51	68.69	4.78	3.38	0.61	0.60	5.60	5.59	1.89
q4	16.44	16.48	68.89	4.75	3.40	0.49	0.48	5.62	5.61	2.12
q5	33.84	33.76	74.27	4.94	4.20	0.58	0.57	6.73	6.76	2.01
q6	33.59	33.58	76.00	5.41	4.29	0.48	0.48	6.77	6.79	2.56
q7	16.07	16.19	71.19	4.19	3.27	0.35	0.34	5.65	5.61	2.07
q8	53.37	53.39	126.97	14.17	5.67	2.15	2.13	28.42	28.44	4.86
q9	17.30	17.23	73.67	5.39	3.72	0.56	0.57	6.03	6.04	2.34
q10	19.51	19.52	116.36	8.95	7.35	0.56	0.57	5.35	5.34	4.03
q11	33.06	33.22	99.98	2.90	11.64	0.27	0.28	8.71	8.65	0.83
q12	33.06	33.10	92.67	2.75	11.51	0.29	0.30	7.90	7.88	0.77
q13	33.59	33.60	73.62	4.33	4.01	0.61	0.60	6.75	6.74	1.61
q14	17.30	17.23	73.67	5.39	3.72	0.56	0.57	6.03	6.04	2.34

Table S3. **Simulated capacitance values.** Capacitances depicted in Fig. S1 simulated with the 3D electrostatic finite element solver Ansys Maxwell for different qubit designs with a convergence accuracy of 10 aF. Differences in the qubit capacitances are due to different sizes of the circuit islands for different designs.

E. Coherence times

A summary of the measured coherence times for 11 GFQ devices is shown in Table S4. We measure the free energy relaxation time T_1 , Ramsey decoherence time T_2^* and echo decoherence time T_2^{echo} . Depending on the qubit, coherence times range from 1 - 10 μs and for each qubit we observe fluctuations in time on the order of microseconds.

The most dominant loss channel for the generalized flux qubits presented in this study is inductive loss, which can be estimated by evaluating Fermi's Golden Rule via

$$\frac{1}{T_1} = \frac{8\pi^3 E_L}{hQ_{\text{ind}}} |\langle 0|\hat{\varphi}|1\rangle|^2 \left(1 + \coth \frac{hf_q}{2k_B T}\right), \quad (\text{S4})$$

where E_L is the inductive energy, Q_{ind} the inductive quality factor, $\hat{\varphi}$ the flux operator in units of Φ_0 , and f_q the qubit frequency. The measured energy relaxation times correspond to inductive quality factors of the order of 10^5 to 10^6 which is consistent with the expected inductive loss of granular aluminum [38]. The quality factors calculated from the measured energy relaxation times are tabulated in the fifth column in Table S4.

device	T_1 (μs)	T_2^* (μs)	T_2^{echo} (μs)	$Q_{\text{ind}}(\times 10^6)$
q1	7.6 / 9.8 / 4.7 / 3.2 \pm 0.3	5.7 / 2.1 / –	10.8 / 12.6 / 3.0	0.9 / 1.16 / 0.56 / 0.38
q2	10.3	2.0	–	1.57
q3	2.4	–	–	1.31
q4	1.3	2.1	–	1.27
q5	4.3	2.4	–	0.90
q7	8.0 \pm 2.4	6.0	7.7	0.61
q8	1.4	2.3	–	0.07
q10	4.1	–	–	0.56
q11	10.5 / 9.9 / 6.7 / 6.2 \pm 0.4	5.6 / 2.6 / –	– / 4.8 / 10.2	1.03 / 0.97 / 0.66 / 0.61
q13	4.4	1.4	–	0.28
q15	15.3 \pm 2.1	9.1	–	–

Table S4. **Measured coherence times at the half-flux sweet spot for different samples.** For measurements with a statistically relevant amount of repetitions we show the mean value and standard deviation. Values separated by forward slashes are taken from different cooldowns, several months apart and measured in different sample holders. In between cooldowns the samples have been stored in ambient conditions.

F. Pulse calibration

We fine-tune the π -pulse amplitude by minimizing the beating pattern in the qubit population measured after a sequence of n successive pulses. Three typical measurements are shown in Fig. S6a. The qubit population vs. pulse number is given by

$$P(n) = a \left(\frac{1}{2} - \frac{1}{2} \cos(\pi n + 2\pi f n) \right) \exp(-\gamma n) + o, \quad (\text{S5})$$

where f is the frequency of the beating and γ accounts for energy decay. The amplitude a and offset o account for measurement errors. Using the parameters extracted from a fit of the data using Eq. S5, we define the π - pulse fidelity as

$$F_\pi(f, \gamma) = (P(1) - P(0))/a = \left(\frac{1}{2} - \frac{1}{2} \cos(\pi + 2\pi f) \right) \exp(-\gamma).$$

In Fig. S6.b we plot $F_\pi(f, \gamma)$ and $F_\pi(f, \gamma = 0)$ for repeated measurements over one hour. While the pulse calibration error $F_\pi(f, \gamma = 0)$ drifts in time, the dominant error source is energy decay.

The photon number for the figures in the main text is calibrated using Ramsey interferometry while populating the readout resonator as depicted in Fig. S7.a. We use the linear AC-Stark shift in the dispersive regime

$$\bar{n} = \frac{\delta f}{\chi} \propto P, \quad (\text{S6})$$

where δf is the frequency shift of the qubit and χ is the dispersive shift of the resonator, to relate the circulating photon number \bar{n} to the power of the readout drive P by fitting the Ramsey fringes for different P . We apply a linear fit as it is depicted in Fig. S7.b.

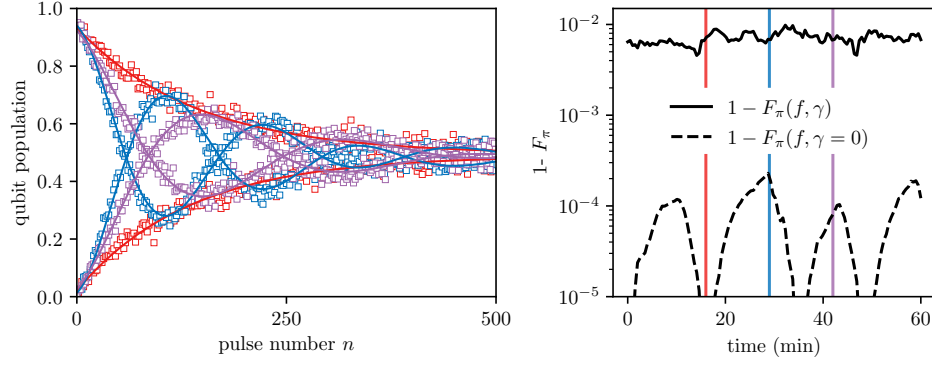


Figure S6. **π -pulse calibration.** **a)** The qubit population is plotted versus a subsequently played number of π -pulses for three individual experiments conducted 13 min apart. Oscillations in this measurement indicate the imperfection of the π -pulse over- or underscoring a perfect bit-flip that sum up to an inversion of the qubit population after half a period of the oscillation. The oscillations are dampened by energy relaxation. **b)** The experiment in **a)** is conducted contiguously over the course of one hour and we plot $F_\pi(f, \gamma)$ and $F_\pi(f, \gamma = 0)$ in continuous and dashed lines, respectively. $F_\pi(f, \gamma = 0)$ drifts continuously with a period of tens of minutes.

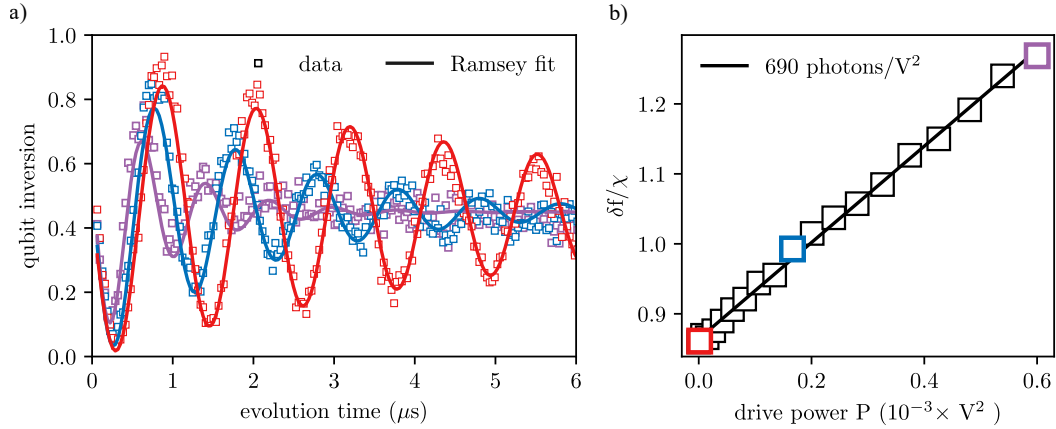


Figure S7. **Photon number calibration.** **a)** Ramsey fringes are recorded while simultaneously populating the readout resonator using different drive powers. The fringes are fitted to a sinusoidal function (continuous lines) to obtain the qubit frequency detuning δf with respect to the qubit pulse. The red markers correspond to no drive and the powers corresponding to the blue and violet points are the same as in panel b. **b)** The linear fit of δf vs. different readout powers (continuous line) gives the photon number calibration used in the main text.